J Mater Sci (2023) 58:9251–9263

Energy materials

Self-healing boron-doped Sb_2Se_3 thermoelectric materials prepared using liquid metallic Ga–Sn alloys

Minsu Kim[1], Dabin Park[1], and Jooheon Kim[1,2,3,*]

[1] School of Chemical Engineering and Materials Science, Chung-Ang University, Seoul 06974, Republic of Korea
[2] Department of Advanced Materials Engineering, Chung-Ang University, Anseong-si, Gyeonggi-do 17546, Republic of Korea
[3] Department of Intelligent Energy and Industry, Graduate School, Chung-Ang University, Seoul 06974, Republic of Korea

Received: 21 February 2023
Accepted: 12 May 2023
Published online: 26 May 2023

ABSTRACT

Inorganic thermoelectric materials are typically brittle and unrecyclable. Among these inorganic thermoelectric materials, antimony selenide (Sb_2Se_3) is a promising material for preparing topological insulators and photovoltaic devices. Sb_2Se_3 has a large Seebeck coefficient and extremely low electrical conductivity. To apply Sb_2Se_3 as a thermoelectric material, its electrical conductivity must be improved, and self-healing must be realized. In this study, we fabricated self-healing thermoelectric composites using liquid metals from Ga–Sn and Sb_2Se_3 thermoelectric materials. Sb_2Se_3 nanowires and nanosheets were fabricated through hydrothermal reactions. To improve the thermoelectric performance, the Sb_2Se_3 nanowire and nanosheet samples were doped with elemental boron. B-doping enhanced both carrier concentration and the carrier mobility, leading to improved electrical conductivity and Seebeck coefficient. The composite material with the highest thermoelectric performance was identified by adjusting the ratio of Sb_2Se_3 nanowires to nanosheets. Subsequently, a liquid metal alloy Ga–Sn was prepared to achieve a melting point of 166 °C. Furthermore, a Ga–Sn and Sb_2Se_3 hybrid composite with a weight ratio of 5:5 was prepared through hot pressing at 130 °C (temperature lower than the melting point). The fabricated composite was cut into two pieces and heated to approximately 130 °C to induce self-healing. The cuts self-healed successfully, albeit with a certain loss of the Ga–Sn alloy. The electrical conductivity of the self-healed composites decreased slightly owing to the presence of voids and losses in the Ga–Sn liquid metal.

Handling Editor: Kevin Jones.

Address correspondence to E-mail: jooheonkim@cau.ac.kr

https://doi.org/10.1007/s10853-023-08593-2

GRAPHICAL ABSTRACT

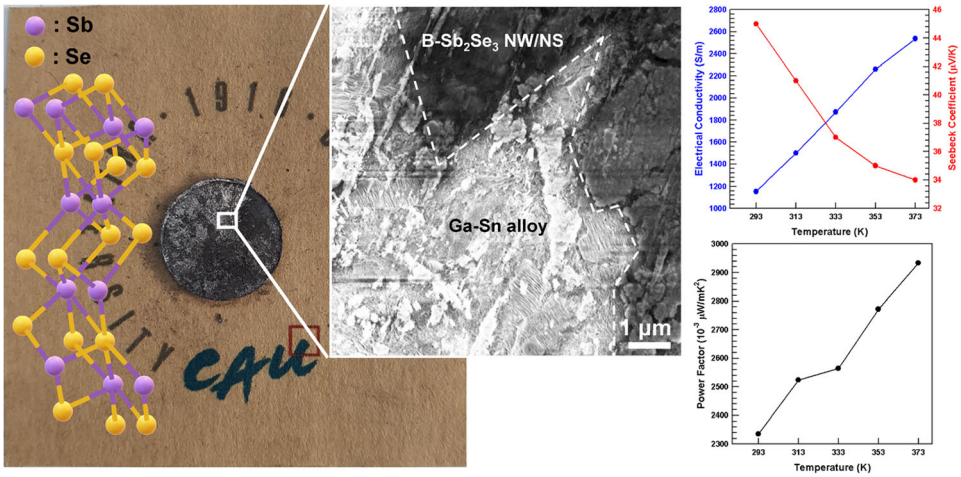

Introduction

In recent decades, Te-based thermoelectric materials, such as Bi_2Te_3 [1–3], Sb_2Te_3 [4–6], and Ag_2Te [7, 8], have attracted considerable research attention owing to their high Seebeck coefficients. Te-based materials can easily be synthesized into diverse structures such as nanowires, nanorods, and nanosheets. However, the toxic nature of Te has prompted research focused on exploring less toxic and earth-abundant Se-based materials that have similar properties [9–12]. Many researchers have investigated Bi_2Se_3- [13, 14], Bi_2O_2Se- [15–18], Cu_2Se- [19–21], and SnSe-based materials [22, 23] to achieve enhanced thermoelectric performances. Among these materials, antimony selenide (Sb_2Se_3) are insulating materials, which has extremely low electrical conductivity and large Seebeck coefficient over 400 μV/K [24–26]. This extremely low electrical conductivity limits its application as a thermoelectric material. Similar to other Se-based thermoelectric materials, Sb_2Se_3 can be synthesized in different structures such as nanosheets [27, 28], nanowires [29, 30], and thin films [25, 31]. Therefore, to enhance the thermoelectric performance of Sb_2Se_3, its electrical conductivity must be increased.

Inorganic thermoelectric materials such as rigid composite or flexible films exhibit several disadvantages such as low durability. Damaged thermoelectric materials cannot be repaired and should be replaced. To overcome this limitation, self-healing thermoelectric materials have been explored. Self-healing properties have been induced by introducing organic materials [32, 33], polymer materials [34–36], phase-change materials [37], and liquid metals [38, 39]. Unlike organic or polymeric materials, liquid metals can enhance the electrical conductivity of thermoelectric materials. A liquid metal that is commonly used is eutectic gallium–indium (EGaIn), which has a low melting point of 15.7 °C [40, 41]. Owing to this low melting point, EGaIn is easy to process; however, the operating temperature range is reduced because the operating temperature (T_{op}) must typically be lower than the melting point (T_{mp}) (*i.e.*, $T_{op} < T_{sh} < T_{mp}$). Malakooti et al. fabricated EGaIn-embedded thermoelectric supercooling materials, which can freeze temperature to − 84 °C [42]. And Chen et al. fabricated flexible thermoelectric generator with bismuth telluride and bismuth antimony telluride nanowires and EGaIn contacts. The fabricated thermoelectric generator produced 127 nW at a 32.5 K temperature difference [43]. However, compared to our study, EGaIn liquid metal was used to connect electrically each generator legs in series. In this study, we use Ga–Sn alloys with a melting point of 166 °C. The melting points of gallium and tin are 32 °C and 232 °C, respectively. The melting point of the alloy can be controlled by adjusting the ratio of Ga and Sn contents.

The high melting point and electrical conductivity of the liquid metal Ga–Sn alloy can help enhance the thermoelectric performance of Sb_2Se_3 composites. To establish the transport network of charge carriers to promote the recovery of the cut plane of the composite, Sb_2Se_3 nanowire and nanosheet composites are fabricated, and their thermoelectric performances are evaluated. The highest composite ratio is selected to fabricate a self-healing Ga–Sn@B-Sb_2Se_3 composite. When the composite is cut into two pieces and heated to 130 °C, the Ga–Sn alloy melts at the cut surface, and the cut surface is restored.

Experiments

Materials

Antimony (III) chloride ($SbCl_3$; 99%) and sodium selenite (Na_2SeO_3; anhydrous; 99%) were purchased from Alfa Aesar. Boric acid (BH_3O_3; 99.5%), sodium borohydride ($NaBH_4$; 98%), tin (Sb; shot, 99.999%), and gallium (Ga; 99.99%) were obtained from Sigma–Aldrich. Hydrazine monohydrate and cetyltrimethylammonium bromide (CTAB; 99%) were purchased from Daejung Chemical & Metals Co., Ltd (Seoul, Korea). Potassium antimony tartrate ($C_8H_4K_2O_{12}Sb_2 \cdot 3H_2O$; 99.5%) was acquired from FUJIFILM Wako Pure Chemical Corporation (Osaka, Japan). All reagents were used as received without any purification process.

Synthesis of Sb_2Se_3 nanowires and nanosheets

In 100 mL of distilled water (D.I. Water), 0.665 g of antimony potassium tartrate, and 0.51 g of sodium selenite were dissolved with vigorous magnetic stirring. The color of the solution approached white with stirring. Subsequently, 20 mL of hydrazine monohydrate was added to the solution, and the color became peach-like. The peach-colored solution was transferred to a Teflon-lined autoclave with 40 mL of tetrahydrofuran to fill 80% of the container. The sealed autoclave was heated at 135 °C for 9 h. The product was washed with ethanol and D.I. water several times, and then dried in a vacuum oven at 60 °C overnight to obtain Sb_2Se_3 nanowires [44].

The synthesis procedure of Sb_2Se_3 nanosheets were referred previously reported studies [28]. Sb_2Se_3 nanosheets were synthesized by the following process: 0.3423 g of antimony trichloride and 0.3375 g of CTAB were dissolved in 45 mL D.I. water. Subsequently, 0.3891 g of sodium selenite and 0.3390 g of sodium borohydride were dissolved in another 50 mL D.I. water. These two solutions were mixed separately with magnetic stirring for 30 min, and then, mixed together followed by 30 min of magnetic stirring to obtain a homogenous solution. The obtained solution was transferred to a 200-mL Teflon-lined autoclave, and D.I. water was added to fill approximately 70% of the autoclave. The autoclave was placed in a drying oven and heated to 200 °C for 24 h. The product was washed with ethanol and D.I. water several times, and then dried in a vacuum oven at 60 °C overnight to obtain Sb_2Se_3 nanosheets.

To dope Sb_2Se_3 nanowires and nanosheets, each nanowire and nanosheet materials was added to 1 M of H_3BO_3 (boric acid) solution for 6 h and dried overnight.

Fabrication of Ga–Sn alloys and Ga–Sn@B-Sb_2Se_3 composites

To fabricate the Ga–Sn alloy, Ga and Sn elements were mixed in various ratios. Each mixture was poured into a ceramic crucible and shifted to a muffle furnace purged with N_2 gas. Considering the melting point of Sn (232 °C), the muffle furnace was heated to 235 °C at a rate of 3 °C min^{-1}. After melting Ga and Sn, the temperature of the muffle furnace was gradually decreased to room temperature to obtain the Ga–Sn alloy. Subsequently, differential scanning calorimetry (DSC; DSC 131 Evo, Setaram Instrumentation) was performed to determine the melting point of the Ga–Sn alloys.

The Ga–Sn@B-Sb_2Se_3 composites were fabricated by mixing the Ga–Sn alloy and Sb_2Se_3 nanowire/nanosheet mixture with a weight ratio of 1:1 and hot-pressing at 130 °C for 20 min to fabricate disk-shaped pellets.

Characterization

The morphology and microstructures of the Sb_2Se_3 nanowires and nanosheets were investigated using field-emission scanning electron microscopy (FE-SEM; SIGMA) and field-emission transmission electron microscopy (FE-TEM; JEM-F200). Moreover, the elemental mappings of the samples were obtained

using energy-dispersive X-ray spectroscopy (EDS; Thermo NORAN System 7, SIGMA) with FE-TEM. The crystalline structures of the Sb_2Se_3 nanowires and nanosheets were confirmed using X-ray diffraction (XRD; D8 Advance, AXS Bruker) over a 2θ range of 10° to 80° at 40 kV and 40 mA at a scan rate of 0.1° s^{-1} under λ = 0.154056 nm Cu K_α radiation. The binding energies of Sb_2Se_3 nanowires and nanosheets were determined using X-ray photoelectron spectroscopy (XPS; K-Alpha, Thermo UK) using a 1486.6 eV Al K_α X-ray source. The chemical structures in the samples were clarified using a Raman spectrometer II (DXR2xi, Thermo) with a near-infrared laser operating at 532 nm and a charge-coupled device detector.

The thermoelectric property S and σ values of the samples were measured using a homemade device. Specifically, the homemade device with a pair of voltmeters was used to implement a four-probe method. A pair of thermostats was used to quantify the σ between 298 and 373 K. The S value was calculated using the following equation:

$$S = \Delta V/\Delta T \quad (1)$$

where ΔV is the change in the thermal electromotive force, and ΔT is the temperature difference. The thermoelectric power force (PF) was calculated as follows:

$$PF = S^2 \cdot \sigma \quad (2)$$

In order to increase the accuracy of electrical conductivity and Seebeck coefficient measurement, each measurement was repeated more than 10 times, and the average value is shown in the figure of the manuscript.

In addition, the melting point of the Ga–Sn alloy was measured using DSC.

The charge carrier concentration and mobility were measured using Hall-effect measurements (HMS-300, Ecopia) under ± 1 T magnetic field with the van der Pauw method at room temperature.

Results and discussion

Thermoelectric performances of B-doped Sb_2Se_3 nanowires and nanosheets

Figure 1 shows the thermoelectric Seebeck coefficients and electrical conductivity of Sb_2Se_3 nanowires and nanosheets before and after B-doping. The thermoelectric performances with increasing Sb_2Se_3 nanosheet ratios were measured. The pristine Sb_2Se_3 particles exhibited a high Seebeck coefficient of 400 μV/K at room temperature, which indicated that Sb_2Se_3 is a p-type thermoelectric material with hole charge carriers [44]. The Seebeck coefficient of the Sb_2Se_3 nanosheets was higher than that of the nanowires. In general, one-dimensional nanowire/nanorod materials act as more effective transport channels for charge carriers compared with two-dimensional nanosheet materials and thus have a high electrical conductivity but low Seebeck coefficient. The pristine Sb_2Se_3 exhibited an extremely low electrical conductivity (10^{-4} Sm^{-1}), owing to which, Sb_2Se_3 was considered to be a promising material for topological insulators. After B doping, the Seebeck coefficient and electrical conductivity increased slightly for both the nanowire and nanosheet samples. B is a representative p-type dopant that affects the charge carrier concentration and mobility. The carrier concentration and mobility of Sb_2Se_3 nanowire was 6.24×1011 cm^{-3} and 10 cm^2 V^{-1} s^{-1}, respectively. The electrical conductivity of B-doped Sb_2Se_3 nanowires and nanosheets increased owing to the increase in the carrier concentration and mobility. The measured carrier concentration and mobility of Sb_2Se_3 nanowires were 2.69×10^{13} cm^{-3} and 37 cm^2V^{-1} s^{-1}. Due to the enhancement of carrier concentration and mobility, the power factor of Sb_2Se_3 composite was improved as a whole nanosheet ratio, and the highest power factor value of 3.22×10^{-3} μW/mK^2 was obtained at the 3:7 ratio of nanosheet and nanowire.

To confirm the synthesis of B-doped Sb_2Se_3, XRD and Raman analyses were performed, as shown in Fig. 2. The XRD patterns of both Sb_2Se_3 nanowire and nanosheets corresponded to the previously reported XRD pattern of Sb_2Se_3 (JCPDS No. 15–0861) [44, 45]. The hkl index for Sb_2Se_3 nanowires is shown in Fig. S1. No other secondary peaks were observed, which indicated the successful synthesis of each nanowire and nanosheet. After B-doping, the XRD patterns shifted to slightly lower angles. This phenomenon likely occurred owing to the introduction of B atoms between the lattices of Sb_2Se_3, resulting in lattice expansion. The Scherrer equation, $t = 0.94 \times \lambda/B\cos(\theta)$, was used to check grain size of Sb_2Se_3 nanowire using XRD patterns, where t is the grain size, λ denotes the X-ray wavelength

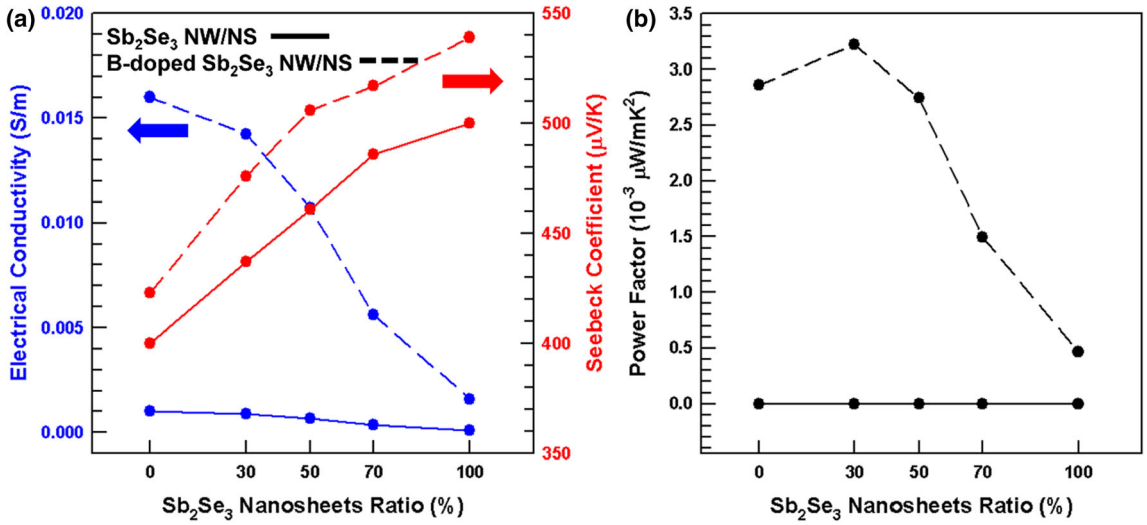

Figure 1 **a** Electrical conductivity and Seebeck coefficient, **b** calculated power factor of Sb_2Se_3 composites with various Sb_2Se_3 nanosheets ratio measured at room temperature.

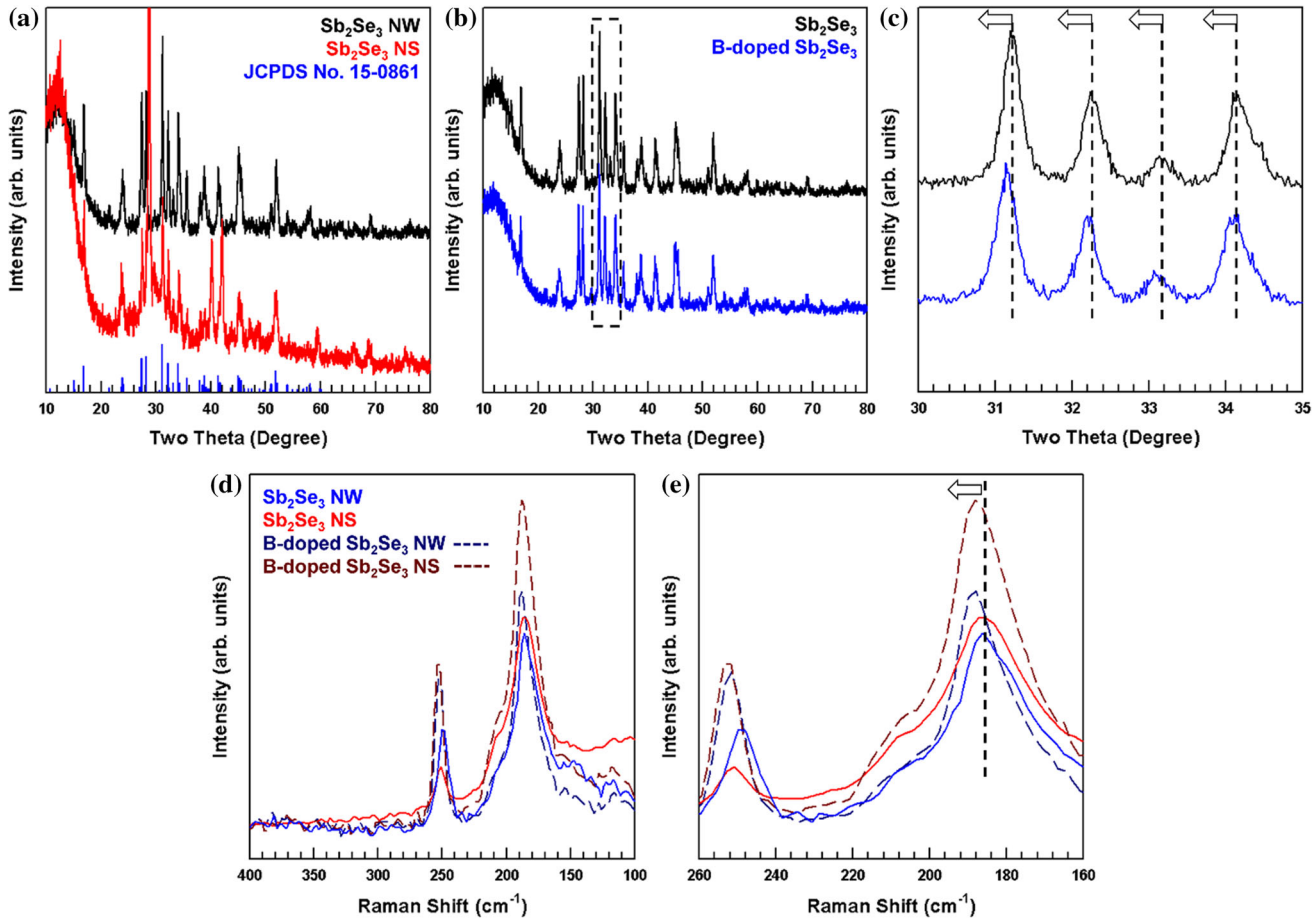

Figure 2 XRD patterns of **a** Sb_2Se_3 nanowires, nanosheets and **b** B-doped Sb_2Se_3. **c** High-resolution XRD pattern of **b**. **d** Raman spectra and **e** high-resolution of Sb_2Se_3 nanowires, nanosheets, B-doped nanowires, and nanosheets.

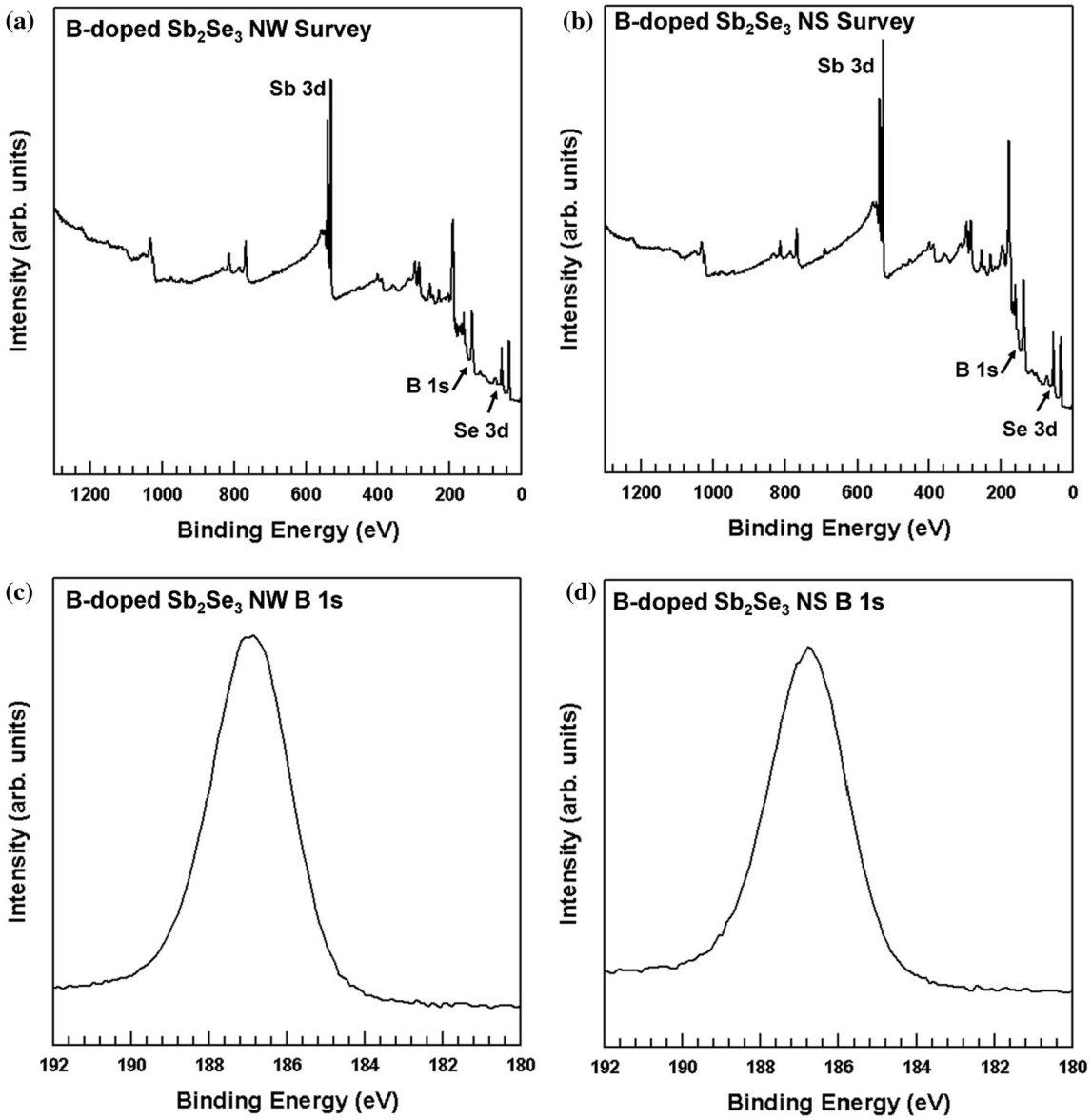

Figure 3 XPS survey spectra of **a** B-doped Sb_2Se_3 nanowire **b** B-doped Sb_2Se_3 nanosheets. High-resolution B 1 s XPS spectra of **c** B-doped Sb_2Se_3 nanowires and **d** B-doped Sb_2Se_3 nanosheets.

(0.154056 nm), and *B* is the full width at half-maximum XRD peak width in radians [46]. The calculated grain size of Sb_2Se_3 nanowires was 27 ± 3 nm, which corresponding to the diameter of nanowires from FE-SEM images discussed below. For nanosheet material, nanosheets were easily aggregated to form 5–600 nm size. After boron doping, the XRD peak was shifted slightly, and the morphology and diameter of nanowire were almost unchanged. For this reason, it is not sufficient to confirm boron doping using the change of grain size. However, boron doping was confirmed with Raman, XPS analyses and expansion of lattice fringe in FE-TEM measurement which discussed below. Similarly, the Raman spectra of the Sb_2Se_3 nanowire and nanosheets corresponded to the Raman signature peaks of Sb_2Se_3 located at 188, 208, and 252 cm^{-1}, respectively [47]. After B-doping, the Raman peaks exhibited a blue shift, indicating the expansion of the Sb_2Se_3 lattice [48]. An XPS analysis was conducted to examine the surface chemistry of B-doped Sb_2Se_3. Figure 3 shows the XPS survey spectra of the B-doped Sb_2Se_3 nanowires and nanosheets. After B-doping, a B 1 s peak emerged located at 187 eV indicating B (0) state [49].

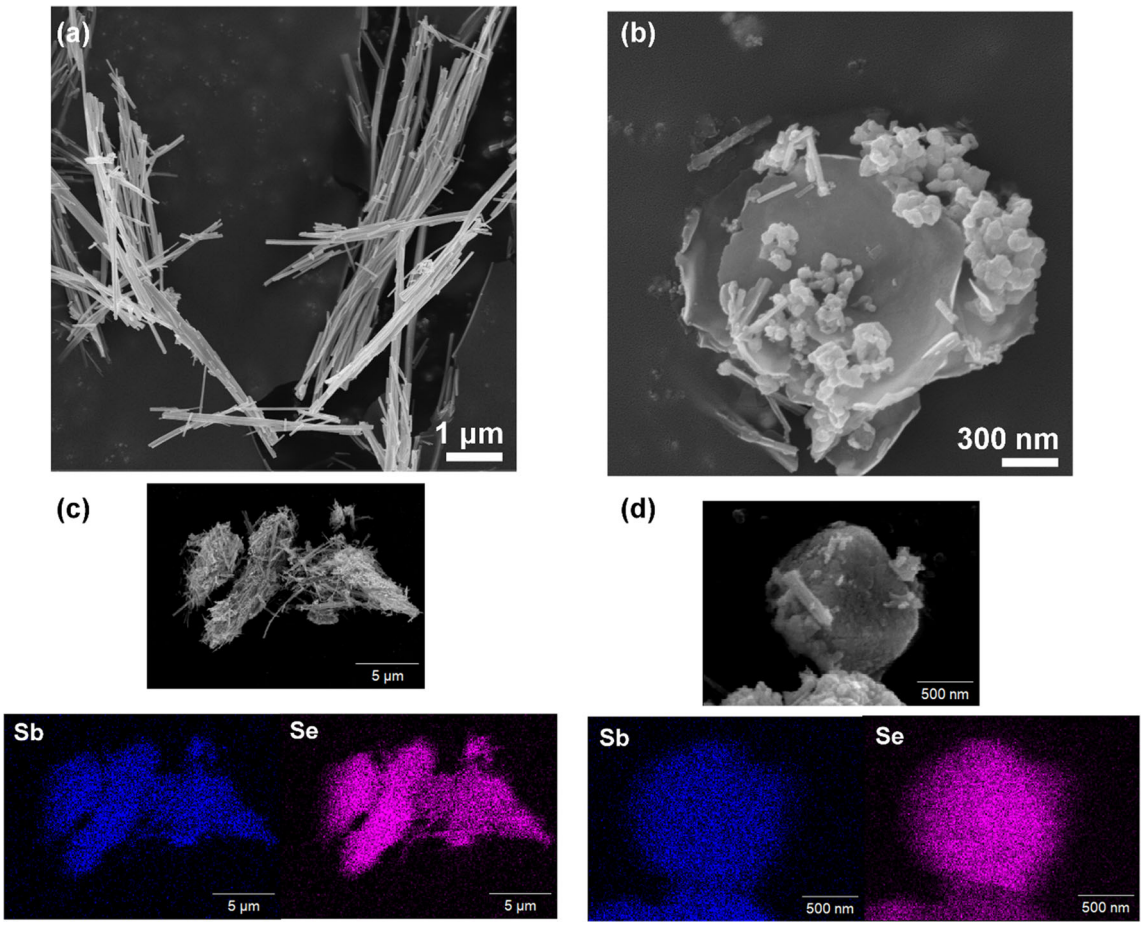

Figure 4 FE-SEM images of **a** Sb_2Se_3 nanowires and **b** Sb_2Se_3 nanosheets. EDS elemental mappings of **c** Sb_2Se_3 nanowires and **d** Sb_2Se_3 nanosheets.

FE-SEM and FE-TEM analyses were performed to examine the morphology and B-doping. The FE-SEM images of the Sb_2Se_3 nanowires and nanosheets indicated the presence of highly crystalline structure, consistent with the XRD patterns. The Sb_2Se_3 nanowires exhibited a thin and long morphology with a diameter and length of 25–30 nm and 5–6 μm, respectively. The size of the Sb_2Se_3 nanosheets was 5–600 nm. The EDS elemental mapping indicates that the Sb_2Se_3 nanowires and nanosheets were successfully synthesized. The FE-TEM images also indicated that the Sb_2Se_3 nanowires had a highly crystalline wire morphology with a lattice fringe of 0.397 nm. The Sb_2Se_3 nanosheets had a size of 5–600 nm with a lattice fringe of 0.216 nm. After B-doping, the lattice fringes of the Sb_2Se_3 nanowires and nanosheet expanded to values of 0.416 nm and 0.229 nm, respectively. As mentioned previously, the introduction of B atoms between the Sb_2Se_3 lattice led to lattice expansion. EDS elemental mapping was performed to confirm successful B-doping. For both the nanowire and nanosheet samples, the Sb and Se elements were uniformly distributed with a stoichiometric ratio of 2:3 confirmed by XPS data. Furthermore, the B elements were randomly distributed, indicating successful B-doping (Figs. 4, 5).

Fabrication of Ga–Sn liquid metal alloys and performance evaluation of Ga–Sn@B-Sb_2Se_3 composites

To fabricate the Ga–Sn alloy with a melting point of 166 °C, Ga and Sn were melted in a ceramic crucible by maintaining a temperature of 235 °C (higher than the melting point of Sn, i.e., 232 °C) for 2 h and then allowing it to naturally decrease to room temperature. The DSC curve was obtained to confirm the melting point of the Ga–Sn alloy. The melting points of Ga and Sn were 32 and 232 °C, respectively, as shown in Fig. 6. For various ratio of Ga and Sn, the

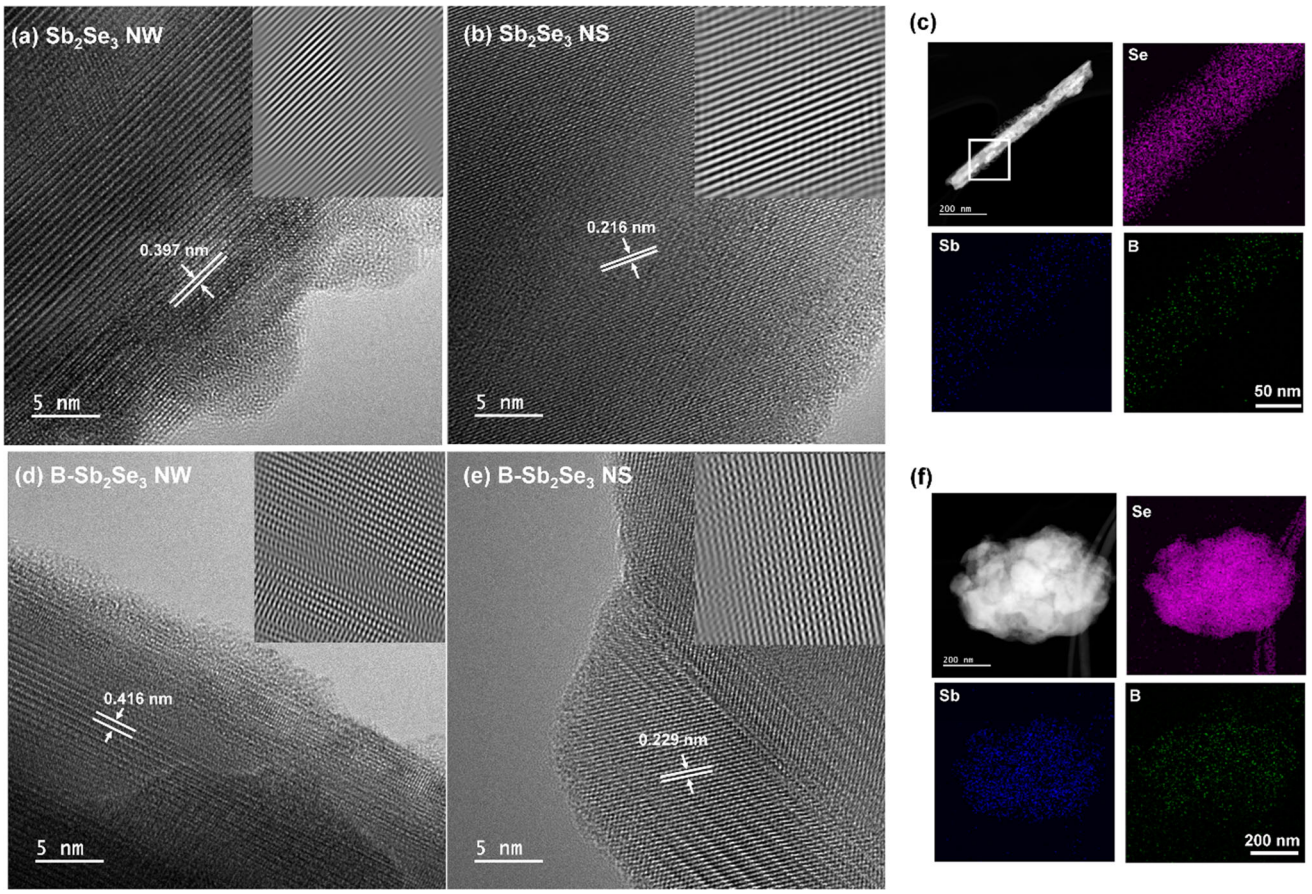

Figure 5 High-resolution FE-TEM images of **a** Sb_2Se_3 nanowires, **b** Sb_2Se_3 nanosheets, **d** B-doped Sb_2Se_3 nanowires, and **e** B-doped Sb_2Se_3 nanosheets (Inset: inverse fast Fourier transform image). EDS elemental mapping of **c** B-doped Sb_2Se_3 nanowires and **f** B-doped Sb_2Se_3 nanosheets.

melting points were located between the melting points of Ga and Sn. For a self-healing material, the self-healable temperature range of the liquid metal should be above the operating temperature and below the melting point (*i.e.*, $T_{op} < T_{sh} < T_{mp}$). If the operating temperature (T_{op}) is above the self-healable temperature (T_{sh}), the liquid metal materials (in this study; Ga–Sn alloys) that exist in the solid state can leak out of the composite as they begins to change to a liquid phase. Considering the performance of the thermoelectric materials in the low temperature range, the melting point of the Ga–Sn alloy was set to approximately 166 °C by adjusting the ratios of Ga and Sn. When the Ga and Sn ratio was 1:3, the melting point was 166 °C, as shown in Fig. 6.

Before fabricating the self-healing Ga–Sn@B-Sb_2Se_3 composites, the B-doped Sb_2Se_3 nanowires and nanosheets were mixed in various ratio, and the corresponding thermoelectric performances were evaluated. As shown in Fig. 1, the composite with a nanowire and nanosheet ratio of 7:3 exhibited the highest power factor value of 3.22×10^{-3} μW/mK^2. Using this configuration, the Ga–Sn alloy and Sb_2Se_3 NW/NS with a weight ratio of 5:5 were hot-pressed at 130 °C for 20 min to fabricate disk-shaped pellets. The hot-pressed temperature was selected by considering DSC results as shown in Fig. 6. Because Ga–Sn alloys starts to melt over 120 °C, not a fully melting, the operating temperature of 130 °C can make Ga–Sn particles injected into the B-Sb_2Se_3 composites. A high proportion of liquid metal in the Ga–Sn@B-Sb_2Se_3 composite is required for a successful self-healing process. When the composite was cut, self-healing of the composite occurred during the process of melting and solidifying the liquid metal at the cross section. In addition, as the content of liquid metal in the composite increases, the electrical conductivity increases but the Seebeck coefficient

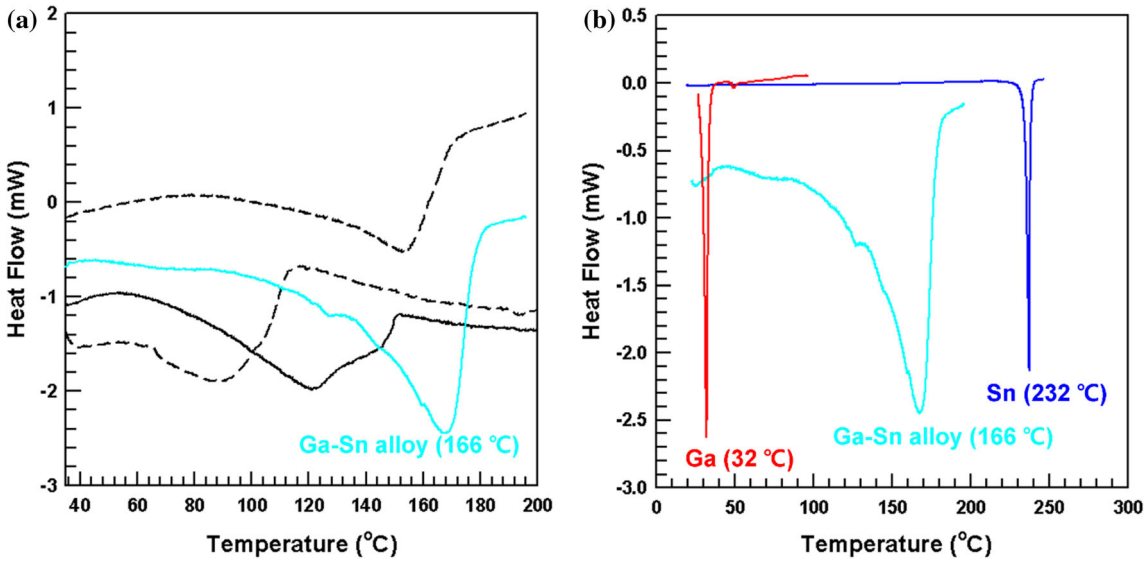

Figure 6 DSC curves of **a** Ga–Sn alloys with various ratio and **b** Ga (red line), Sn (blue line), and Ga–Sn alloys used in this study (sky blue line).

decreases, so the composite was manufactured by selecting a ratio of 1:1 in consideration of this. Because the melting point of Ga–Sn alloy was approximately 166 °C and self-healing was expected to occur at a lower temperature, the thermoelectric performance of the Ga–Sn@B-Sb_2Se_3 composite was evaluated at lower temperatures (up to 100 °C). As shown in Fig. 7(a,b), owing to the high electrical conductivity of the metal elements Ga and Sn, the electrical conductivity increased, and the Seebeck coefficient decreased. The highest power factor value was 2932×10^{-3} μW/mK^2, which is 910 times higher than B-doped Sb_2Se_3 nanowires and nanosheets composite with a ratio of 7:3. To confirm the self-healing properties, the Ga–Sn@B-Sb_2Se_3 composite was cut into two pieces. The cut surface was attached and heated to 150 °C. Before and after the self-healing process, FE-SEM images were recorded to confirm that the cut surface self-healed through the melting of the Ga–Sn alloy (Fig. 8). After self-healing, the relative electrical conductivity and Seebeck coefficient were measured again at 373 K to confirm the performance stability as shown in Fig. 7(c). The results indicated that the electrical conductivity slightly decreased owing to losses in the liquid metal melting and solidification processes and as the self-healing process was repeated, the electrical conductivity gradually decreased while Seebeck coefficient was almost unchanged. Due to these changes in electrical conductivity and Seebeck coefficient, the power factor of the composite decreased with cycles. Through several cycles, liquid metal loss occurred, which can be seen as reducing the power factor value. However, the power factor of the composite maintained 96% value after 5 self-healing cycles.

In this work, we fabricated Ga–Sn alloys and Ga–Sn@B-Sb_2Se_3 composites with enhanced thermoelectric performances with B-doping and reusable property. The Sb_2Se_3 nanowires and nanosheets composites show extremely low electrical conductivity; however, the electrical conductivity was greatly improved by doping with element B and introducing Ga–Sn liquid metal. The liquid metal acts as a path of carriers and when the composite is damaged, it acts as a self-healing agent by applying heat to melt Ga–Sn alloys. Unlike conventional thermoelectric devices that could not heal damage, liquid metal was introduced to improve performance and introduce self-healing ability, which can be applied to other thermoelectric devices operating at low temperatures.

Conclusions

We fabricated a self-healing thermoelectric composite using a liquid metal alloy Ga–Sn and Sb_2Se_3 thermoelectric materials. Boron doping was performed

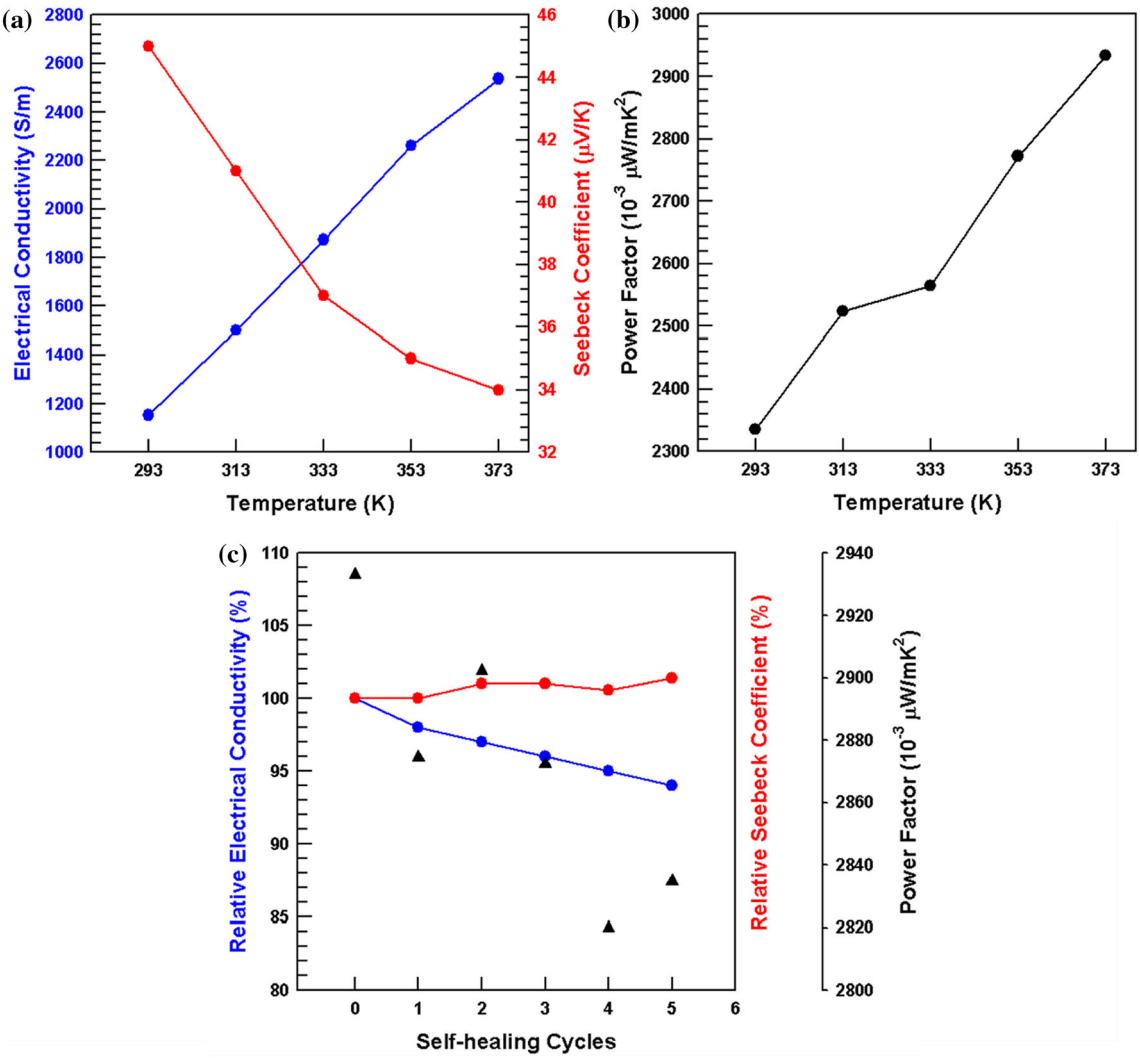

Figure 7 **a** Electrical conductivity and Seebeck coefficient, **b** calculated power factor of Ga–Sn@B-Sb_2Se_3 composites with increasing temperature. **c** Relative electrical conductivity, Seebeck coefficient, and calculated power factor of Ga–Sn@B-Sb_2Se_3 composites with self-healing cycles at 373 K.

for both the Sb_2Se_3 nanowire and nanosheets samples to enhance their thermoelectric performance by modifying carrier concentration and mobility. B-doping enhanced the carrier concentration and carrier mobility, which led to improved electrical conductivity and Seebeck coefficient. By adjusting the Sb_2Se_3 nanowire and nanosheet ratios, the composite with the highest thermoelectric performance was identified. By B-doping, Raman spectra shows blue shift, which indicating the expansion of Sb_2Se_3 lattice. This expansion of lattice was also confirmed by checking lattice fringe expansion of each Sb_2Se_3 nanowire and nanowires. To give self-healable property for Sb_2Se_3 composite, liquid metal was chosen to also improve electrical conductivity. The self-healable property should be performed above the thermoelectric operating temperature and below the melting point of liquid metal (*i.e.*, $T_{op} < T_{sh} < T_{mp}$). Subsequently, the liquid metal alloy Ga–Sn was fabricated to achieve a melting point of 166 °C, which exceeds the set operating temperature of 100 °C. Ga–Sn alloy and Sb_2Se_3 hybrid composites with a weight ratio of 1:1 were fabricated through hot-pressing at a temperature lower than the melting point (166 °C). The power factor of Ga–Sn@B-Sb_2Se_3 composite was improved to 2932×10^{-3} μW/mK^2 which is 910 times higher than B-doped Sb_2Se_3 nanowires and nanosheets composite with a ratio of 7:3. To confirm the self-

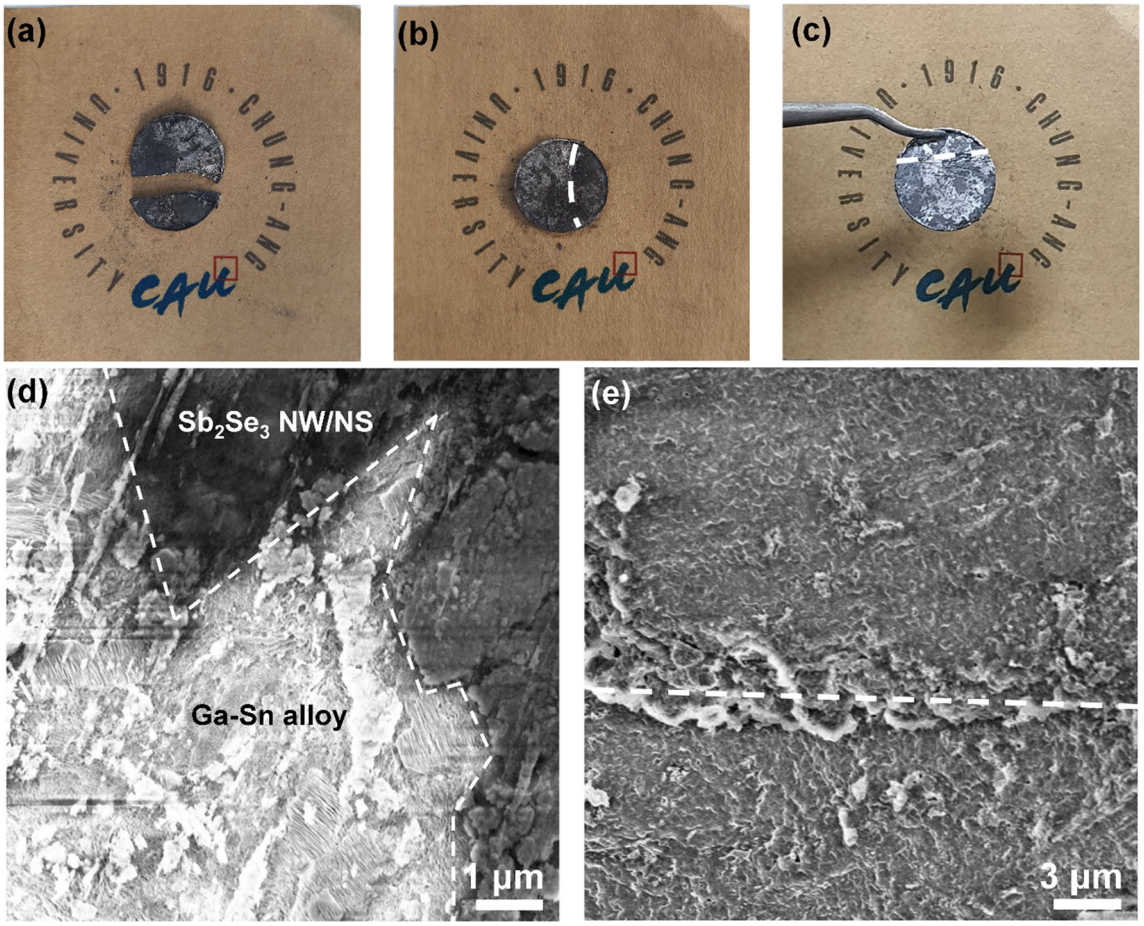

Figure 8 Photos of Ga–Sn@B-Sb_2Se_3 composites **a** cut in two, **b** reattached by heating to 150 °C and **c** self-healing composite lifted using tweezers. FE-SEM images of Ga–Sn@B-Sb_2Se_3 composites **d** before and **e** after self-healing process.

healable property, the fabricated composite was cut into two pieces and heated at approximately 150 °C to induce self-healing. The truncated sections self-healed successfully, albeit with a certain loss of Ga–Sn. The electrical conductivity of the composite after self-healing slightly decreased owing to the presence of voids and loss of Ga–Sn liquid metal. The power factor of Ga–Sn@B-Sb_2Se_3 composite maintained over 96% after 5 self-healing cycles.

Acknowledgements

This work was supported by the Human Resources Development (No. RS-2023-00244347) of the Korea Institute of Energy Technology Evaluation and Planning(KETEP) grant funded by the Korea government Ministry of Trade, Industry and Energy and also supported by the MSIT (Ministry of Science and ICT), Korea, under the ITRC (Information Technology Research Center) support program (IITP-2021-2020-0-01655) supervised by the IITP (Institute of Information & Communications Technology Planning & Evaluation).

Author contributions

MK performed conceptualization, investigation, writing—original draft, data curation, formal analysis, and methodology. DP did investigation, data curation, and formal analysis. Prof. JK done supervision and project administration.

Declarations

Conflict of interest On behalf of all authors, the corresponding author states that there is no conflict of interest.

Data and Code Availability Not Applicable.

Ethical approval Not Applicable.

Supplementary Information: The online version contains supplementary material available at https://doi.org/10.1007/s10853-023-08593-2.

References

[1] Hong M, Chen Z-G, Zou J (2018) Fundamental and progress of Bi2Te3-based thermoelectric materials. Chin Phys B 27:048403

[2] Scheele M, Oeschler N, Meier K, Kornowski A, Klinke C, Weller H (2009) Synthesis and thermoelectric characterization of Bi2Te3 nanoparticles. Adv Funct Mater 19:3476–3483

[3] Mamur H, Bhuiyan M, Korkmaz F, Nil M (2018) A review on bismuth telluride (Bi2Te3) nanostructure for thermoelectric applications. Renew Sust Energ Rev 82:4159–4169

[4] Yang J, Cao J, Han J, Xiong Y, Luo L, Dan X et al (2022) Stretchable multifunctional self-powered systems with Cu-EGaIn liquid metal electrodes. Nano Energy 101:107582

[5] Zhu P, Imai Y, Isoda Y, Shinohara Y, Jia X, Zou G (2005) Enhanced thermoelectric properties of PbTe alloyed with Sb2Te3. J Phys Condens Matter 17:7319

[6] Das D, Malik K, Deb A, Dhara S, Bandyopadhyay S, Banerjee A (2015) Defect induced structural and thermoelectric properties of Sb2Te3 alloy. J Appl Phys 118:045102

[7] Wang X-Y, Wang H-J, Xiang B, Fu L-W, Zhu H, Chai D et al (2018) Thermoelectric performance of Sb2Te3-based alloys is improved by introducing PN junctions. ACS Appl Mater Interfaces 10:23277–23284

[8] Hu H, Xia K, Wang Y, Fu C, Zhu T, Zhao X (2021) Fast synthesis and improved electrical stability in n-type Ag2Te thermoelectric materials. J Mater Sci Technol 91:241–250

[9] Zhu T, Bai H, Zhang J, Tan G, Yan Y, Liu W et al (2020) Realizing high thermoelectric performance in Sb-doped Ag2Te compounds with a low-temperature monoclinic structure. ACS Appl Mater Interfaces 12:39425–39433

[10] Tiekink ER (2012) Therapeutic potential of selenium and tellurium compounds: opportunities yet unrealized. Dalton Trans 41:6390–6395

[11] Guin SN, Chatterjee A, Negi DS, Datta R, Biswas K (2013) High thermoelectric performance in tellurium free p-type AgSbSe2. Energy Environ Sci 6:2603–2608

[12] Shi Y, Sturm C, Kleinke H (2019) Chalcogenides as thermoelectric materials. J Solid State Chem 270:273–279

[13] Zhao T, Zhu H, Zhang B, Zheng S, Li N, Wang G et al (2021) High thermoelectric performance of tellurium-free n-type AgBi1-xSbxSe2 with stable cubic structure enabled by entropy engineering. Acta Mater 220:117291

[14] Yang Y-X, Wu Y-H, Zhang Q, Cao G-S, Zhu T-J, Zhao X-B (2020) Enhanced thermoelectric performance of Bi2Se3/TiO2 composite. Rare Met 39:887–894

[15] Zhang L, Shang H, Huang D, Xie B, Zou Q, Gao Z et al (2022) N-type flexible Bi2Se3 nanosheets/SWCNTs composite films with improved thermoelectric performance for low-grade waste-heat harvesting. Nano Energy 104:107907

[16] Kim M, Park D, Kim J (2021) Enhancement of Bi2O2Se thermoelectric power factor via Nb doping. J Alloys Compd 851:156905

[17] Tan X, Liu Y, Liu R, Zhou Z, Liu C, Lan JL et al (2019) Synergistical enhancement of thermoelectric properties in n-Type Bi2O2Se by carrier engineering and hierarchical microstructure. Adv Energy Mater 9:1900354

[18] Yang F, Wu J, Suwardi A, Zhao Y, Liang B, Jiang J et al (2021) Gate-Tunable polar optical phonon to Piezoelectric scattering in few-layer Bi2O2Se for high-performance thermoelectrics. Adv Mater 33:2004786

[19] Zheng Z-h, Wang T, Jabar B, Ao D-w, Li F, Chen Y-x et al (2021) Enhanced thermoelectric performance in n-Type Bi2O2Se by an exquisite grain boundary engineering approach. ACS Appl Energy Mater 4:10290–10297

[20] Qin Y, Yang L, Wei J, Yang S, Zhang M, Wang X et al (2020) Doping effect on Cu2Se thermoelectric performance: a review. Materials 13:5704

[21] Fan P, Huang X-l, Chen T-b, Li F, Chen Y-x, Jabar B et al (2021) α-Cu2Se thermoelectric thin films prepared by copper sputtering into selenium precursor layers. Chem Eng J 410:128444

[22] Choo S, Ejaz F, Ju H, Kim F, Lee J, Yang SE et al (2021) Cu2Se-based thermoelectric cellular architectures for efficient and durable power generation. Nat Commun 12:1–11

[23] Burton MR, Mehraban S, Beynon D, McGettrick J, Watson T, Lavery NP et al (2019) 3D printed SnSe thermoelectric generators with high figure of merit. Adv Energy Mater 9:1900201

[24] Zhang J, Zhang T, Zhang H, Wang Z, Li C, Wang Z et al (2020) Single-crystal SnSe thermoelectric fibers via laser-induced directional crystallization: from 1D fibers to multidimensional fabrics. Adv Mater 32:2002702

[25] Mavlonov A, Razykov T, Raziq F, Gan J, Chantana J, Kawano Y et al (2020) A review of Sb2Se3 photovoltaic absorber materials and thin-film solar cells. Sol Energy 201:227–246

[26] Chen S, Liu T, Zheng Z, Ishaq M, Liang G, Fan P et al (2022) Recent progress and perspectives on Sb2Se3-based photocathodes for solar hydrogen production via photoelectrochemical water splitting. J Energ Chem 67:508–523

[27] Fan P, Chen G-J, Chen S, Zheng Z-H, Azam M, Ahmad N et al (2021) Quasi-vertically oriented Sb2Se3 thin-film solar cells with open-circuit voltage exceeding 500 mV prepared

via close-space sublimation and selenization. ACS Appl Mater Interfaces 13:46671–46680
[28] Wang J, Rehman SU, Xu Y, Zuo B, Cheng H, Guo L et al (2022) Two-dimensional antimony selenide (Sb2Se3) nanosheets prepared by hydrothermal method for visible-light photodetectors. Sol Energy 233:213–220
[29] Zhou Y, Feng W, Qian X, Yu L, Han X, Fan G et al (2019) Construction of 2D antimony (III) selenide nanosheets for highly efficient photonic cancer theranostics. ACS Appl Mater Interfaces 11:19712–19723
[30] Ma Z, Chai S, Feng Q, Li L, Li X, Huang L et al (2019) Chemical vapor deposition growth of high crystallinity Sb2Se3 nanowire with strong anisotropy for near-infrared photodetectors. Small 15:1805307
[31] Zhou H, Feng M, Feng M, Gong X, Zhang D, Zhou Y et al (2020) Gradient doping of sulfur in Sb2Se3 nanowire arrays as photoelectrochemical photocathode with a 2% half-cell solar-to-hydrogen conversion efficiency. Appl Phys Lett 116:113902
[32] Duan Z, Liang X, Feng Y, Ma H, Liang B, Wang Y et al (2022) Sb2Se3 Thin-film solar cells exceeding 10% power conversion efficiency enabled by injection vapor deposition technology. Adv Mater 34:2202969
[33] Kee S, Haque MA, Corzo D, Alshareef HN, Baran D (2019) Self-healing and stretchable 3D-printed organic thermoelectrics. Adv Funct Mater 29:1905426
[34] Ataei S, Khorasani SN, Neisiany RE (2019) Biofriendly vegetable oil healing agents used for developing self-healing coatings: A review. Prog Org Coat 129:77–95
[35] Wang S, Urban MW (2020) Self-healing polymers. Nat Rev Mater 5:562–583
[36] Li CH, Zuo JL (2020) Self-healing polymers based on coordination bonds. Adv Mater 32:1903762
[37] Wang Z, Gangarapu S, Escorihuela J, Fei G, Zuilhof H, Xia H (2019) Dynamic covalent urea bonds and their potential for development of self-healing polymer materials. J Mater Chem A 7:15933–15943
[38] Du X, Jin L, Deng S, Zhou M, Du Z, Cheng X et al (2021) Recyclable, self-healing, and flame-retardant solid–solid phase change materials based on thermally reversible cross-links for sustainable thermal energy storage. ACS Appl Mater Interfaces 13:42991–43001
[39] Tutika R, Haque A, Bartlett MD (2021) Self-healing liquid metal composite for reconfigurable and recyclable soft electronics. Commun Mater 2:1–8
[40] Markvicka EJ, Bartlett MD, Huang X, Majidi C (2018) An autonomously electrically self-healing liquid metal–elastomer composite for robust soft-matter robotics and electronics. Nat Mater 17:618–624
[41] Ozutemiz KB, Wissman J, Ozdoganlar OB, Majidi C (2018) EGaIn–metal interfacing for liquid metal circuitry and microelectronics integration. Adv Mater Interfaces 5:1701596
[42] Malakooti MH, Kazem N, Yan J, Pan C, Markvicka EJ, Matyjaszewski K, Majidi C (2019) Liquid metal supercooling for low-temperature thermoelectric wearables. Adv Funct Mater 29:1906098
[43] Chen B, Kruse M, Xu B, Tutika R, Zheng W, Bartlett MD, Wu Y, Claussen JC (2019) Flexible thermoelectric generators with inkjet-printed bismuth telluride nanowires and liquid metal contacts. Nanoscale 11:5222–5230
[44] Kim M, Park D, Kim J (2021) Synergistically enhanced thermoelectric performance by optimizing the composite ratio between hydrothermal Sb 2 Se 3 and self-assembled β-Cu 2 Se nanowires. CrystEngComm 23:2880–2888
[45] Zhang L, Wu K, Yu J, Yu Y, Wei Y (2021) Sb2Se3 films fabricated by thermal evaporation and post annealing. Vacuum 183:109840
[46] Venkidu L, Jain Ruth DE, Veera Gajendra Babu M, Esther Rubavathi P, Dhayanithi D, Giridharan NV, Sundarakannan B (2022) Suppression of intermediate antiferroelectric phase in sub-micron grain size Na0.5Bi0.5TiO3 ceramics. J Mater Sci Mater Electron 33:25006–25024
[47] Kumar A, Kumar V, Romeo A, Wiemer C, Mariotto G (2021) Raman spectroscopy and In situ XRD probing of the thermal decomposition of Sb2Se3 thin films. J Phys Chem C 125:19858–19865
[48] Lee Y, He G, Akey AJ, Si R (2011) Flytzani-Stephanopoulos M Herman IP Raman analysis of mode softening in nanoparticle CeO2− δ and Au-CeO2− δ during CO oxidation. J Am Chem Soc 133:12952–12955
[49] Feng B, Zhang J, Zhong Q, Li W, Li S, Li H et al (2016) Experimental realization of two-dimensional boron sheets. Nat Chem 8:563–568